Journal of Geodesy (2001) 75: 99–108

Journal of Geodesy

Arcsecond-level pointing calibration for ICESat laser altimetry of ice sheets

M. E. Lisano[1], B. E. Schutz[2]

[1] Jet Propulsion Laboratory, 4800 Oak Grove Drive, Pasadena, CA 91109, USA, e-mail: mike.lisano@jpl.nasa.gov
Tel.: 818 354 0765; Fax: 818 393 6388
[2] Center for Space Research, University of Texas at Austin, Austin, TX, USA, e-mail: schutz@csr.utexas.edu
Tel.: 512 471 4267

Received: 28 April 2000 / Accepted: 6 November 2000

Abstract. Arcsecond-level accuracy of NASA's ICESat (Ice, Cloud, and land Elevation Satellite) satellite laser altimeter beam pointing angle is required to satisfy the scientific goal of detecting centimeter-level elevation changes, over time, in the Greenland and Antarctic ice sheets. Two different approaches, termed "topographic inferred" and "direct detection", were examined for calibrating the laser pointing angle (that is, detecting and removing pointing determination bias) at the 1.5-arcsec level, using information independent of the onboard pointing instrumentation. Both approaches entail estimating the beam pointing by differencing the three-dimensional position of the altimeter instrument and the laser-beam spot (or "footprint") location on the ground. Analytical assessments of the two approaches are discussed, along with recommendations for the ICESat pointing determination calibration strategy.

Key words: ICESat – GLAS – Calibration – Pointing determination – Ice-sheet altimetry

1 Introduction

The research reported here is an assessment of methods for calibrating the pointing angle measurement made by subsystems of a satellite laser altimeter, which will be deployed on NASA's ICESat (Ice, Cloud, and land Elevation Satellite) spacecraft. ICESat will be one of an assortment of satellites being launched between 1999 and 2002, comprising the space segment of the Earth Observing System (EOS). The EOS is part of an international effort to monitor changes in the Earth's atmosphere, oceans, and ecosystems. The Geoscience Laser Altimeter System (GLAS) carried on ICESat will support the synoptic measurement of semi-decadal changes in the mass of ice contained in the Earth's two great continental ice sheets, located upon Greenland and Antarctica. The altimeter height measurements will be used to determine the topography of the ice sheets with decimeter accuracy over a five-year satellite lifetime.

Two approaches will be used to analyze the altimeter data and extract elevation change: crossovers and profile comparisons. Both approaches are dependent on data collected at different times, thereby providing the basis for determination of temporal changes. In essence, the sum of changes in elevation over the entire ice sheet should indicate the net change of volume of the ice sheet. The mass balance of the continental ice sheets will be inferred from a net change in the volume of the ice sheets (GLAS Science Team 1999).

GLAS will be the first satellite-borne altimeter specifically designed for study of the polar ice sheets. The ICESat/GLAS mission, orbit, and spacecraft/instrument parameters are summarized in Table 1, and specifications for tracking and navigating the ICESat spacecraft are given in Table 2. The ICESat ground-track is designed to repeat exactly once every 183 days, having a near-repeat subcycle with a 25-day period. In addition, ICESat will have a post-launch calibration period lasting 90–120 days, during which the satellite will be maintained in an 8-day repeat ground-track. During this period, it is planned to verify and calibrate the altimeter onboard pointing determination by collecting data at pre-selected calibration sites along the ground-track. The rest of this paper discusses approaches to performing this pointing knowledge calibration.

2 Pointing estimation error and satellite laser altimetry

In this work, we treat the satellite laser altimeter measurement as a vector quantity. The magnitude of the *altimeter measurement vector* is obtained from the round-trip laser pulse travel time (scalar altitude). The vector direction is obtained from the onboard beam

Correspondence to: M. E. Lisano

Table 1. ICESat mission specifications

Scheduled launch	Fall 2001
Mission duration	3 years/5-year goal (follow-on instruments to extend data time series to >1 decade)
"Mean" orbital altitude	600 km
Orbit inclination	94°
Orbit eccentricity (frozen)	0.0013
Groundtrack repeat period	183 days
Orbit determination (radial accuracy)	< 5-cm RMS
Orbit determination (horizontal)	< 20-cm RMS
Sample rate	40 Hz
Laser type	Near-infrared (1.064 μm)
Height measurement precision requirement (1σ)	10 cm
Laser pointing knowledge requirement (1σ)	1.5 arcsec

pointing instrumentation. When combined with the GLAS position vector obtained from precision orbit determination (POD), the geocentric location of the illuminated spot on the surface can be inferred. Figure 1 shows the relationships between the inferred surface height (h_{surface}) and three GLAS data types: the satellite height above a reference ellipsoid, $H_{\text{altimeter/ell}}$ (obtained from POD); the altimeter height measurement, H_{measured} (obtained from the laser round-trip time); the estimated altimeter beam pointing angle, $\delta\alpha_{\text{est}}$ (obtained from the attitude/pointing instrumentation); and the error $\Delta\delta\alpha$ in $\delta\alpha_{\text{est}}$.

A non-zero pointing determination error $\Delta\delta\alpha$ results in erroneous interpretation of the altimeter measurement vector. That is, the range to the surface in estimated beam pointing direction $\delta\alpha_{\text{est}}$ is interpreted as H_{measured}, instead of the actual value H_{true}. The relationship between the measured range H_{measured} and the true range H_{true}, given $\delta\alpha_{\text{est}}$, $\Delta\delta\alpha$, and local ground slope Θ, is given by Eq. (1), which is obtained with a straightforward trigonometric derivation

$$\frac{H_{\text{measured}} - H_{\text{true}}}{H_{\text{true}}} = \frac{\cos(\Theta + \delta\alpha_{\text{est}}) - \cos(\Theta + \delta\alpha_{\text{est}} - \Delta\delta\alpha)}{\cos(\Theta + \delta\alpha_{\text{est}} - \Delta\delta\alpha)} \quad (1)$$

Table 2. ICESat spacecraft design specifications

Tracking systems	2 onboard, dual-frequency GPS receivers 1 satellite laser ranging cube-corner reflector
Communications	S-band and X-band
Attitude determination for control	Two charged-couple display (CCD) star cameras plus gyroscopes
Attitude control technique	Momentum wheels; magnetic torquer bars
Attitude control precision capability	≈20 arcsec (1σ)
Pointing determination	Stellar reference system and laser reference system

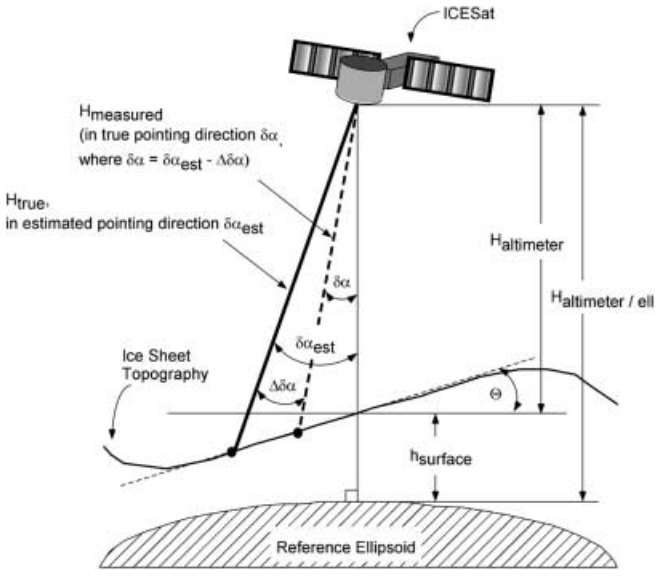

Fig. 1. Laser altimeter measurement of topographic elevation (H_{true} = true range; H_{measured} = measured range; $H_{\text{altimeter}}$ = true altimeter height above direct nadir surface; $H_{\text{altimeter/ell}}$ = true altimeter height above reference ellipsoid; h_{surface} = surface height above reference ellipsoid; Θ = surface slope at measured site; $\delta\alpha$ = true beam pointing angle; $\delta\alpha_{\text{est}}$ = estimated beam pointing angle; $\Delta\delta\alpha$ = error in beam pointing angle)

From Eq. 1, for the nominal ICESat orbital altitude of 600 km, it is observed that $\Delta\delta\alpha = 1$ arcsec causes a range error of about 5.1 cm per degree of combined ground slope and estimated beam pointing angle ($\Theta + \delta\alpha_{\text{est}}$). Compare this pointing-induced height measurement error with the GLAS height measurement error budget in Table 3 (Schutz 1998a). The stringent pointing requirement appearing in the error budget motivates the development of methods to verify and calibrate the beam pointing measurement, that is, to detect and remove systematic bias in the onboard beam pointing determination that is greater than 1.5 arcsec.

The laser altimeter will create an illuminated spot on the ground, or footprint, with a nominal diameter of 60–70 m. The altimeter pointing knowledge will be calibrated by combining the three-dimensional location of the instrument at the time a single laser pulse was fired (obtained, for example, from orbit determination) with the three-dimensional location of the centroid of the resulting laser altimeter footprint. For 1.5-arcsec accuracy, given an ICESat altitude of 600 km, the root-sum-squared (RSS) error in the combined estimates of the satellite and footprint centroid horizontal positions

Table 3. GLAS single-shot error budget (1° surface slope)

Source	1-σ error (cm)
Instrument precision	10
Radial orbit determination	5
Pointing determination	7.5
Troposphere delay	2
Atmospheric scattering	2
Other (mass-center location, etc.)	1
RSS	13.8

should not exceed a horizontal distance of 4.5 m. Experience with the TOPEX spacecraft and simulation studies indicate that sub-decimeter-level three-dimensional orbit determination for ICESat can be achieved based on GPS carrier-phase data (Schutz et al. 1994; Rim et al. 1996). Hence, most of the 4.5-m horizontal error budget falls to the estimation of the footprint centroid position. In addition, precise timing of the footprint detection event is required to compute the satellite position at pulse transmit time with sufficient accuracy. For example, 5 μs of footprint detection time error results in less than 5 cm of ICESat along-track uncertainty.

The GLAS Science Team is planning several approaches for determining footprint locations; two of these approaches will be considered here. The first approach, called "topographic inferred", is to estimate the footprint locations on well-surveyed topography, given the satellite ephemeris and height measurements. The second approach, "direct detection", is based on sensing the footprints using such means as an airborne infrared camera or an array of ground-based photodetectors.

3 Topographic-inferred approach

The topographic-inferred pointing calibration approach is to determine the footprint centroid location based on the use of reference topographic elevations for some preselected, precisely surveyed region, along with estimated satellite position and altimeter height measurements for the same region. The precise reference elevations may be obtained with precise, rapid surveying techniques using global positioning system (GPS) data, such as the real-time kinematic and rapid-static techniques, or with properly-calibrated airborne laser altimetry.

The precision of the topographic-inferred beam pointing estimate is limited by errors in the altimeter height measurements, spacecraft position estimate, time-tag, and reference elevation values. Note that for a single value of terrain slope, the direction of the estimated pointing error will be ambiguous, as there are two possible footprint locations on a sloped surface for a given height measurement and spacecraft location. To assist in resolving such ambiguities, the region over which the calibrations are performed should consist of terrain with multiple footprint sites, each of which is sloped in a different direction. A minimum of two such sites, each having a surface normal vector with unique down-track and along-track components, will permit unambiguous determination of the along-track and down-track components of the beam pointing angle.

The topographic-inferred approach entails reconstructing the beam pointing angle using the estimated position of the altimeter satellite (from precision orbit determination), the estimated elevation of the ground at the footprint (from a precise survey of the calibration site), and the altimeter measurement. The resulting estimated angle $\delta\alpha_{\text{est}}$ will vary from the true angle $\delta\alpha$ by an amount that depends on $\delta\alpha$, as well as ground slope Θ, altimeter height H above the surface, radial orbit determination error Δz_{sat}, ground elevation survey error Δz_{g}, and altimeter measurement error δh. See Fig. 2 for a depiction of how these quantities relate to the estimated angle $\delta\alpha_{\text{est}}$.

From Fig. 2, the true and estimated pointing angles are

$$\begin{aligned}\delta\alpha &= 180^\circ - (90^\circ + \Theta) - \beta_1 = (90^\circ - \Theta - \beta_1)\\ \delta\alpha_{\text{est}} &= 180^\circ - (90^\circ + \Theta) - \beta_2 = (90^\circ - \Theta - \beta_2)\end{aligned} \tag{2}$$

so the error in the beam pointing estimate is given by

$$\Delta\delta\alpha = \delta\alpha_{\text{est}} - \delta\alpha = (\beta_1 - \beta_2) \tag{3}$$

From Eq. (2), angle β_1 can be written as

$$\beta_1 = (90^\circ - \Theta - \delta\alpha) \tag{4}$$

Next, from the law of sines, it is easily proven that

$$R = H\frac{\cos\Theta}{\cos(\Theta + \delta\alpha)} \tag{5}$$

Also from the law of sines

$$\frac{H - \Delta z_{\text{g}} + \Delta z_{\text{sat}}}{\sin(\beta_2)} = \frac{R + \delta h}{\cos(\Theta)} = \frac{H}{\cos(\Theta + \delta\alpha)} + \frac{\delta h}{\cos(\Theta)} \tag{6}$$

Finally, solving Eq. (6) for β_2, and substituting into Eq. (3) along with Eq. (4), yields an expression for the error in the topographic beam pointing estimate

$$\Delta\delta\alpha = 90^\circ - (\Theta + \delta\alpha) - \sin^{-1}\left\{\frac{(H - \Delta z_{\text{g}} + \Delta z_{\text{sat}})\cos(\Theta)\cos(\Theta + \delta\alpha)}{H\cos(\Theta) + \delta h\cos(\Theta + \delta\alpha)}\right\} \tag{7}$$

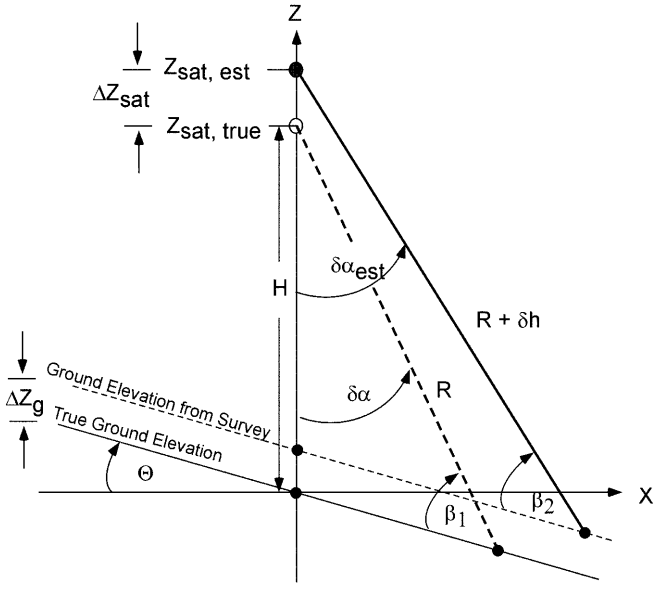

Fig. 2. Geometry of topographic-inferred pointing estimation approach (Δz_{sat} = radial satellite orbit determination error; ΔZ_{g} = ground elevation survey error; R = true range from altimeter to footprint center; $R + \delta h$ = altimeter measurement including noise δh; H = true altimeter height over surface; $\delta\alpha$ = true beam pointing angle; $\delta\alpha_{\text{est}}$ = topographic estimate of beam pointing angle; Θ = ground slope)

We employed a Monte-Carlo analysis of Eq. (7) to determine the effect of sub-satellite ground slope on the attainable accuracy of the topographic-inferred approach. In the analysis, Δz_{sat}, Δz_g, and δh were dispersed as zero-mean, non-cross-correlated Gaussian variates. The variates were each dispersed to 50 random values, with standard deviations as given in Table 4. In this manner, 125 000 combinations of (Δz_{sat}, Δz_g, δh) were generated to create 125 000 dispersed values of $\Delta\delta\alpha$, for each given set of non-dispersed parameters (H, $\delta\alpha$, Θ). Altitude H was set to the GLAS nominal value of 600 km for all cases. Ground slope Θ was evaluated using values ranging from 0.1° to 9.0°. Beam pointing $\delta\alpha$ was evaluated at values of 0 arcsec and ± 20 arcsec. As $\delta\alpha$ appears in Eq. (7) only in terms containing ($\Theta + \delta\alpha$), varying $\delta\alpha$ by only ± 20 arcsec has a negligible effect on $\Delta\delta\alpha$ for the considered range of ground slopes.

The root mean square (RMS) for 125 000 resulting values of $\Delta\delta\alpha$ was computed for each value of ground slope Θ. Figure 3 shows a plot of RMS $\Delta\delta\alpha$, versus ground slope, for $\delta\alpha = 0$ arcsec.

From Fig. 3, the required ground slope value resulting in an RMS $\Delta\delta\alpha$ sufficient for 1.5 arcsec calibration precision, 1σ (point A in Fig. 3) is approximately 2°. For 1.5 arcsec precision 2σ (point B), the required ground slope is approximately 3.7°. For 1.5 arcsec precision 3σ (point C), the required ground slope is approximately 5.9°.

In summary, to make use of topographic calibration for ICESat, the findings of this simple geometric analysis are that: (1) the surveyed calibration site terrain should be sloped by 2° or more, for the calibration precision to be 1.5 arcsec 1σ, and (2) the site should consist of terrain that is sloped in multiple directions with respect to the ground-track. Zwally et al. (1981) noted that approximately 12% of the Greenland and Antarctic ice sheets are sloped by 1° or more. Hence, the number of sufficiently-sloped calibration sites available on the ice sheets may be limited. However, topographic calibration could also be performed in regions other than the ice sheets.

Table 4. Standard deviation values for Gaussian dispersed inputs to the Monte-Carlo analysis of the precision of the topographic-inferred approach

1-σ quantity	Value (cm)	Comment
$\sigma_{\Delta zsat}$	5	From radial orbit determination component of GLAS single-shot error budget
$\sigma_{\delta h}$	10	From instrument error component of GLAS single-shot error budget
$\sigma_{\Delta Zg}$	10	Conservative value representing vertical RMS error for GPS kinematic or static survey methods (cf. Neumann et al. 1996)

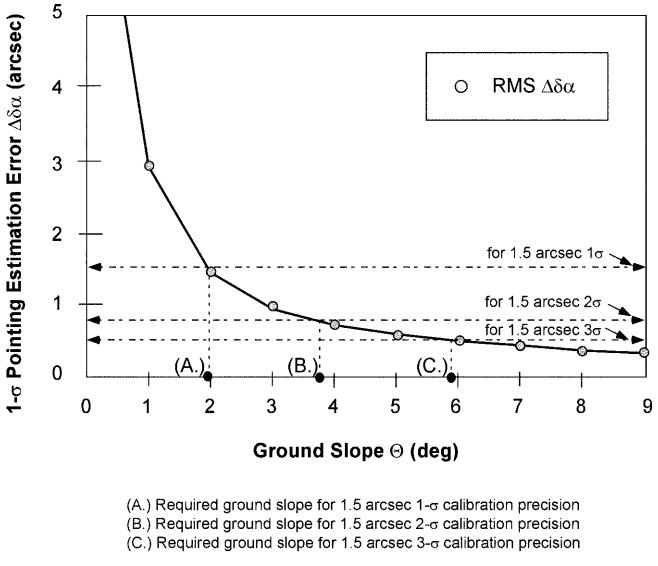

Fig. 3. RMS topographic pointing estimation error $\Delta\delta\alpha$ versus terrain ground slope Θ

4 Direct-detection approaches

Direct-detection calibration approaches involve imaging a laser footprint on the ground. We considered two approaches: use of an imaging camera situated above the spot (e.g. carried on an aircraft) and implementation of an upward-looking "camera" located on the Earth's surface. In the latter case, the camera is constructed with a grid of light detectors, thereby emulating a raster-style camera where each raster is represented by a detector. In the following discussion, the former approach is referred to as the "elevated camera" and the latter approach is the "ground camera".

The elevated camera approach entails flying an aircraft over an expected footprint occurrence site at the time of ICESat overflight. The camera would be pointed at the site, taking the image of one or more footprints by triggering the shutter shortly before the expected appearance of the spots on the ground. The images would be processed by comparing the footprint with landmarks of known size and location that also appeared in the image.

There are many technical and operational difficulties with implementing this approach. For example, since ICESat is moving at about 7 km/s, the passage of the spacecraft over a 3-km-long segment lasts for less than 0.5 s. Thus, a key operational difficulty with the elevated camera approach is timing the aircraft arrival at the site. Technical challenges with the approach include accurate camera pointing from a moving aircraft, and synchronizing the triggering of the camera shutter with the footprint occurrences. Other issues include discerning the footprint in images made during the day, when infrared noise due to sunlight will be at a maximum, or, conversely, discerning both the footprint and landmarks in images made at night. Deploying artificial landmarks, e.g. precisely surveyed infrared beacons, placed in a pattern on the ground along the ICESat calibration-period ground-track, could enhance the elevated camera method in the night overflight scenario. A night overflight with beacons would appear to be the most promising way to implement the elevated camera approach, but addition of the surveyed network of beacons

这个系数模拟的第一个目的是，在给定的探测器间隔下，估算强度模型误差和测量误差对足印中心精度的影响。第二个目的是确定探测器间隔，最优化足印中心的估算精度。

adds operational and technical complexity to an already-problematic calibration approach. While these problems might be overcome with engineering effort, we explored the ground camera approach as a potentially more accurate and more tractable technique.

The ground camera consists of a network of upward-pointed infrared photodetectors capable of measuring the arrival of photons ("on") or no arrival ("off"). In addition, the detectors may measure the intensity of the arriving photons. The detectors would be organized in a uniform array, with each detector designed to record an autonomous indication of photon arrival, or connected to a computer via cabling or wireless radio-frequency connection to record the arrival.

For the ground-camera approach, it is crucial that the detector array be positioned upon, or sufficiently near, the predicted ICESat ground-track. In addition to having an accurate prediction of the ground-track location, establishing the array will require a high-precision surveying campaign. The array must be sufficiently wide in the cross-track direction to compensate for possible errors in the predicted footprint position in the Earth-fixed cross-track direction, as well as long enough in the along-track direction to sample at least one footprint.

Hence, the agile off-nadir pointing capability of the ICESat spacecraft is an important element. The 20-arcsec 1-σ pointing control accuracy, about ± 60 m on the surface, provides a bound for the size of the calibration area. For example, the pointing control capability suggests that the minimum cross-track width can be about ± 180 m (3σ), assuming sub-meter-level prediction error in ICESat coordinates. However, since the shot-to-shot distance is 170 m, the minimum along-track length should also be 240 m to image one entire footprint with 70-m diameter. Thus, for example, a detector grid that is 240 m (down-track dimension) by 360 m (cross-track dimension) should be able to capture one spot.

Assuming the array is surveyed using precision GPS-based techniques, a significant advantage of the ground-camera approach is that the footprint location can be determined readily in the Earth-fixed WGS-84 reference frame. This is simpler and potentially more precise than the use of imaged landmarks in the elevated-camera method. A disadvantage of the approach is the logistics of deploying and connecting an array of as many as a few hundred detectors at the calibration site. Thus, as discussed in the next section, it was important to assess how many photodetector array elements would be required to determine the beam pointing with the required precision.

5 Detector array parametric simulation study

这部分的目的是进行系数模拟研究，利用探测器阵列模拟结果估算足印中心结果系数和两个因素有关（1）探测器阵列足印的位置
（2）阵列中探测器的间距

This section discusses a parametric simulation study to evaluate footprint centroid estimation with simulated data from an array of detectors. Parameters that were varied were related (1) to the positions of the footprints on a detector array, and (2) to the spacing between detectors in the array. One objective of this parametric study was to assess the effects of intensity model errors and measurement errors on the accuracy of the footprint centroid estimate for a given detector spacing. A second objective was to determine a detector spacing that would optimize the footprint centroid estimation accuracy.

The centroid estimation methods were based on two general categories of data gathered from an array. The first class of data is termed on/off data. It is a binary assertion of whether or not a detector/reflector was illuminated. The second class of data is relative intensity measurement data, which may be obtained by measurement with a detector. 两种数据：（1）开关数据（2）相对强度测量数据

The nominal GLAS footprint size is approximately 70 m. At the time this research was performed, the actual GLAS laser far-field transverse intensity profile was not known. Thus, in the interest of developing and assessing "prototype" intensity-based methods, the footprints were modeled with a Gaussian transverse intensity profile [Eq. (8)]

$$I(r) = I_{\max} \exp\left[-2\frac{r^2}{(70\,\mathrm{m})^2}\right] \tag{8}$$

with $I_{\max} = 1.0$. Here, r is the distance from the detector to the footprint centroid

$$r = \sqrt{(x_{\mathrm{refl}} - x_{\mathrm{centroid}})^2 + (y_{\mathrm{refl}} - y_{\mathrm{centroid}})^2} \tag{9}$$

This is the classical zeroth-order transverse far-field intensity distribution expected for a laser beam (cf. Siegmann 1986).

We developed and tested three centroid estimation methods based on on/off or intensity data. The Method 1 centroid estimation technique uses on/off data, and Methods 2 and 3 use intensity data. Method 1 simply approximates each footprint centroid as the aggregate geometric centroid of the group of polygons (squares and triangles) formed by the illuminated array elements. Method 2 fits intensity data to a Gaussian intensity profile, estimating centroid coordinates (x_c, y_c). Method 3 also fits the intensity data to a Gaussian intensity profile, but estimates four model parameters (x_c, y_c, $I_{\max}$, σ_b). 模拟的开关和强度数据利用三次相同的足印产生

Simulated on/off and intensity data sets were generated with a set of up to three identical simulated footprints. The footprints were modeled as occuring 170 m apart from centroid to centroid, along a "footprint line". Each instance of a footprint line is defined by three parameters: slope m, intercept b, and s_1, the distance along the footprint line from the array y-axis to the first footprint centroid. The fundamental measure of accuracy in the parametric study was the offset O_{ijkn} of the estimated centroid location. Here, subscripts i, j, k, and n are individual-case indices for footprint, slope, intercept, and first-footprint location. O_{ijkn} is defined as the distance between the estimated and true footprint centroid locations for the ith footprint, for footprint line case (m_j, b_k, s_{1n}). The aggregate accuracy of each method, over a set of one-footprint and three-footprint

Table 5. Parametric sweep increments and limits for footprint line intercept (b), slope (m) and first-footprint location (s_1) as a function of array element spacing Δ

	Min	Max	Increment	Increment value
b	−Δ m	0 m	1 m	$N_b = \Delta + 1$
m	0°	15°	1°	$N_m = 16$
s_1	35 m	(35 + Δ) m	1 m	$N_{s_1} = \Delta + 1$

cases, was assessed with a statistical quantity we define as the total mean offset, or TMO

$$\mathrm{TMO} = \frac{1}{N_m N_b N_{s_1}} \sum_{n=1}^{N_{s_1}} \sum_{j=1}^{N_m} \sum_{k=1}^{N_b} \mathrm{MEAN}_{jkn} \tag{10}$$

where

$$\mathrm{MEAN}_{jkn} = \frac{1}{N_{\mathrm{fp}}} \sum_{i=1}^{N_{\mathrm{fp}}} O_{ijkn} \quad \text{估算中心位置的偏移} \tag{11}$$

In Eqs. (10) and (11), N_{fp} is the number of footprints in a single case, N_{m} is the number of footprint line slopes considered, N_b is the number of footprint line intercepts, and N_{s_1} is the number of first-footprint locations. The increments and limits N_{fp}, N_m, and N_{S_1} for sweeping b, m, and s_1 are shown in Table 5.

An example parametric sweep through values of m, b, and s_1 for a three-footprint line is shown in Fig. 4.

The scatter of the offsets about the mean for each case is also characterized in the aggregate sense, in terms of the "total mean standard deviation" (TMSD). The TMSD [Eq. (12)] is defined as the average value for all cases of the RMS difference for each case between the individual footprint offsets O_{ijkn} and the mean MEAN_{jkn}

$$\mathrm{TMSD} = \sum_{n=1}^{N_{s_1}} \sum_{j=1}^{N_m} \sum_{k=1}^{N_b} \left\{ \sum_{i=1}^{N_{\mathrm{fp}}} \frac{(O_{ijkn} - \mathrm{MEAN}_{jkn})^2}{N_{\mathrm{fp}}} \right\}^{1/2} \tag{12}$$

Offset histograms were also used to study the statistical distribution of offsets. This was done to provide a sense of the normality or non-normality of O_{ijkn}, as b, m, and s_1 were varied for a given array geometry. Results of these studies are discussed in the next two sections.

6 On/off data results

We assessed the Method 1 technique of estimating the footprint centroids for three-footprint line cases having parameters swept through ranges described in Table 5. The assessment consisted of first understanding whether Gaussian statistics (mean and standard deviation) could be used to describe the aggregate tendencies of the single-case mean solution offsets, MEAN_{jkn}, then studying the aggregate accuracy of the approach versus element spacing.

Histograms of MEAN_{jkn} [Eq. (11)] were plotted for the different array spacing values. One histogram is shown as an example in Fig. 5, for a square-cell array with 35-m spacing. The histogram shown in Fig. 5 has a single peak visible, at the histogram bin resolution. The distribution is slightly negatively skewed, but approaches a normal distribution, which validates the use of Gaussian statistical measures TMO and TMSD to describe the central tendency and standard deviation of MEAN_{jkn}.

Figure 6 is a plot of TMO and TMSD for Method 1, versus the value of array spacing. In this plot, TMSD is the size of the 1-σ error bar for each data point. The expected general trend is for the accuracy to decrease with an increase in element spacing, corresponding to decreasing data. This trend is seen in Fig. 6. The accuracy of Method 1 starts at approximately 1.36 ± 0.52 m (1σ) for a square-cell array with $\Delta x = \Delta y = 15$ m. The accuracy decreases to 2.43 ± 0.86 m (1σ) for $\Delta x = \Delta y = 20$ m, and to 6.33 ± 2.18 m (1σ) for $\Delta x = \Delta y = 35$ m.

The oscillations in the TMO curve result from the nonlinearity of the Method 1 centroid estimation algorithm. The estimate produced by Method 1 is not only strongly dependent upon the number of illuminated elements, but also a discrete function of the geometry of those elements (which form discrete "point polygons"). In this discrete-geometric sense, TMO and TMSD are

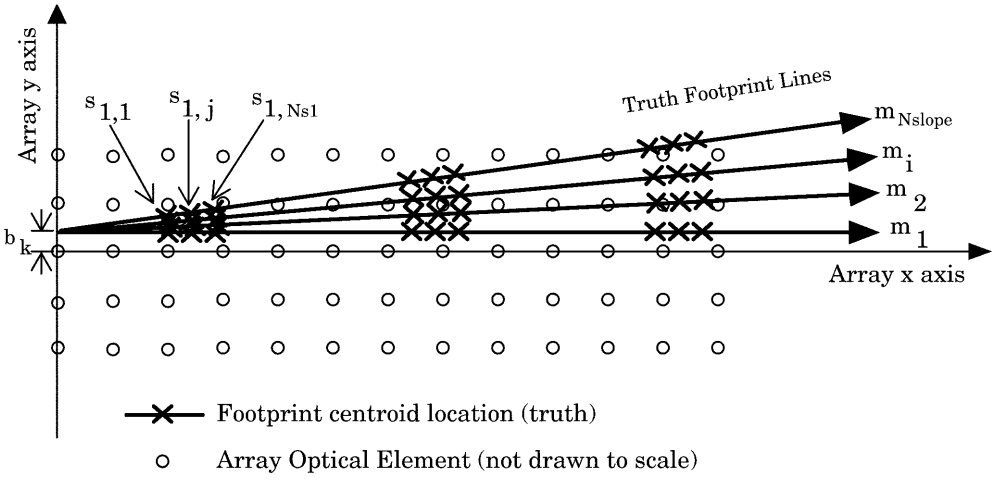

Fig. 4. Three-footprint line parametric sweep through b, m, and s_1 (b = array frame y-axis intercept of footprint line; m = footprint line slope; s_1 = location of first footprint centroid)

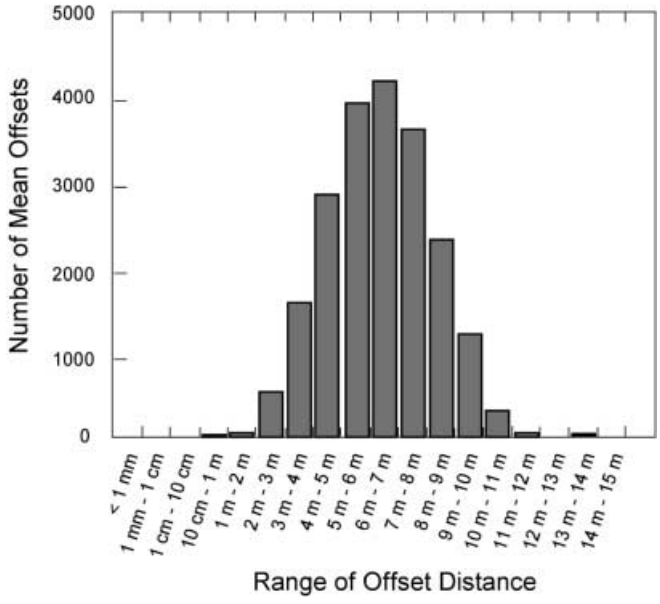

Fig. 5. Histogram of Method 1 mean offsets for "averaging sweep", for three footprints on an array with 35-m spacing

analogues of geometric dilution of precision (GDOP) that is used in GPS accuracy analyses. Lisano discusses a set of studies he performed to verify the geometric origin of the TMO oscillations in his dissertation (Lisano 1995).

With the Method 1 TMO/TMSD curve in Fig. 6, it is possible to establish an element spacing distance Δ, given a desired level of centroid estimate accuracy. The array elements should be spaced no more than 27 m apart for the centroids to be determined with on/off data with better than 4.5-m accuracy, 1σ, by means of Method 1 geometrical estimation. Note that for integer values of spacing from 22 to 25 m, the 1-σ expected accuracy is greater than 4.5 m. To increase the likelihood of attaining 4.5-m accuracy from 1σ to 2σ, the array elements should be spaced no more than 20 m apart.

In summary, on/off data provides the minimum information about the footprint centroid locations that can be obtained with a discrete array of detectors. As a result, it is expected that the accuracy of the footprint centroid estimate based upon on/off data (for example, using the Method 1 semi-geometric estimation algorithm) is a minimum accuracy bound. While the Method 1 centroid estimation routine is coarse relative to intensity data techniques discussed below, it is a more robust algorithm from two standpoints. First, it is immune to errors in the measured intensity, and second, it is not affected by errors in the modeled transverse intensity profile. To verify instrument pointing using this method to an accuracy of 1.5 arcsec, corresponding to 4.5 m of footprint centroid location error, 2σ, the detectors should be spaced no more than 20 m apart.

7 Intensity data results

The Method 2 (estimate x_c and y_c) and Method 3 (estimate x_c, y_c, $I_{\max}$, and σ_b) techniques were evaluated for three-footprint line cases swept through the range of parameters described in Table 5. First, we examined Method 2 and Method 3 centroid estimation benchmark cases, with no intensity model or measurement errors. Estimation errors in this idealized case were expected to depend solely upon the number and geometry of the illuminated detectors within each footprint. Method 2 and Method 3 TMO versus element spacing Δ is plotted in Fig. 7, with a logarithmic ordinate.

As seen in Fig. 7, the Method 2 footprint centroid accuracy (errors due to activated element geometry only) starts at approximately 10 μm for a square-cell array with $\Delta x = \Delta y = 15$ m; it increases monotonically to approximately 3 mm for $\Delta x = \Delta y = 30$ m. The Method 3 footprint centroid determination accuracy starts at approximately 20 μm for a square-cell array with

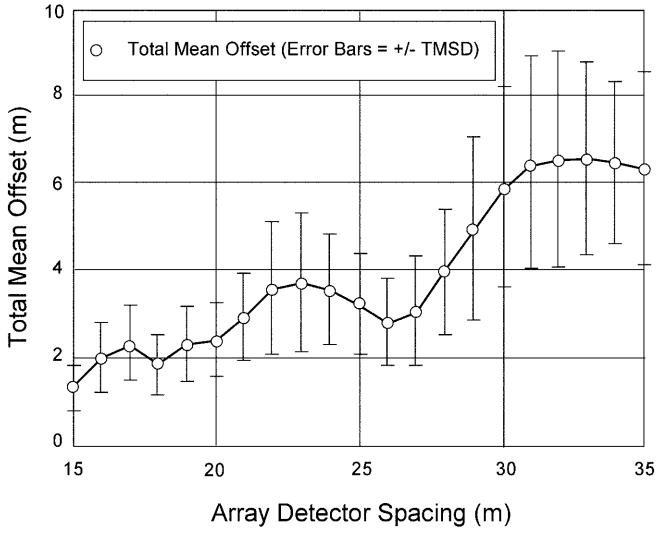

Fig. 6. Method 1 TMO versus element spacing, with TMSD as 1-σ error bars (three footprints illuminate array in all cases)

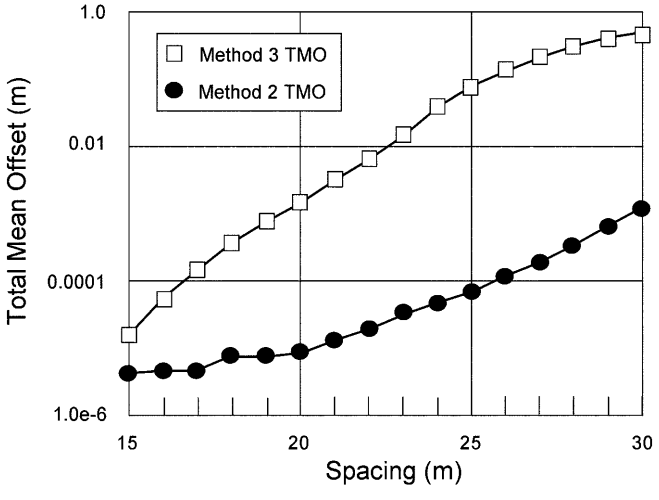

Fig. 7. Method 2 and Method 3 TMO versus element spacing, no intensity model or measurement errors (three footprints illuminate array in all cases)

$\Delta x = \Delta y = 15$ m; it increases to centimeter level for $\Delta x = \Delta y = 21$ m, and begins to exceed 1 m for $\Delta x = \Delta y = 26$ m. Of course, the extremely precise estimates result from the lack of measurement noise or model errors. Method 3 is less accurate than Method 2 because, although there are no simulated model parameter errors, the estimation of I_{max} in Method 3 was initialized using the maximum measured intensity for each footprint.

Next, the effects of multiple error sources were examined. A simulation was performed which included combined measurement errors including: 10-cm RMS random survey errors, detector saturation intensity $= 0.9\ I_{max}$, detector activation threshold intensity $= 0.01 I_{max}$, and beam spreading and intensity attenuation due to laser aperture diffraction and atmospheric turbulence effects. The resulting Method 2 and Method 3 TMO curves from this simulation are shown in Fig. 8.

Figure 8 shows that the accuracy of Method 3 in the presence of these combined errors is constant, and better than Method 2, at the 1-decimeter level for element spacing $\Delta < 22$ m. It is $\approx 0.5 \pm 1.0$ m (2σ) for a 24-m spacing, becoming much larger for higher values of the spacing. The rapid degradation of Method 3 for spacing > 22 m is due to the reduction, on average, in the number of elements per footprint, below the number of parameters estimated with Method 3 (four parameters). However, because Method 2 requires only two or more elements to solve for the two centroid vector components, it provides a better solution than Method 3 for $\Delta > 23$ m. In all Method 2 and 3 cases, the estimation is initialized with an a priori centroid estimate that is accurate to within 10 m, as provided by Method 1.

Given a sufficient number of illuminated detectors per footprint, estimates of altimeter footprint centroid positions based on intensity data are consistently more accurate than those obtained using on/off data. Even when the estimate accuracy is considerably degraded by measurement-related errors and intensity model errors, the Method 2 and Method 3 centroid estimates are accurate at levels better than 1 m. For example, Method 2 enables sub-2-m centroid accuracy (2σ) for element spacings as large as 34 m, and Method 3 enables centroid accuracy of better than 0.2 m (2σ) for spacings of 22 m or smaller. As stated earlier, these two methods assume that the laser footprint has a Gaussian transverse intensity profile.

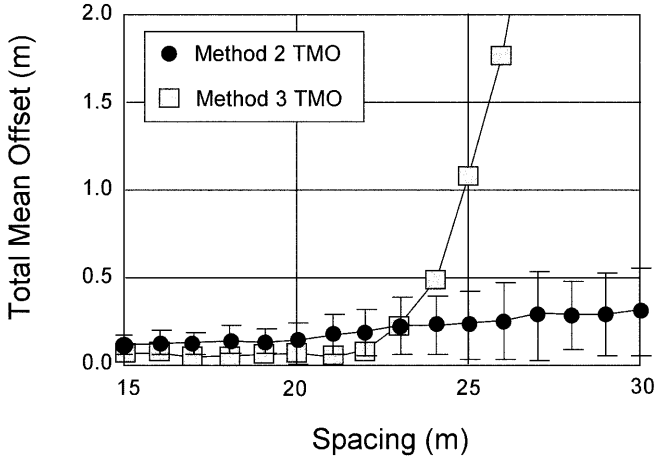

Fig. 8. Combined effects of measurement and model errors on Method 2 and Method 3 TMOs (three footprints illuminate array in all cases)

As stated earlier, the intensity-data-based results reported here serve as a proof-of-concept for intensity-based methods. As the intensity profile of the actual ICESat laser altimeter instrument could be significantly non-Gaussian, these methods should be re-evaluated using models of the actual profile once it is known.

8 Other error sources

As part of this research, we evaluated additional error sources which could affect the topographic-inferred and direct-detection techniques. Of particular concern were unmeasured laser-beam high-frequency vibration, or "jitter", unpredicted systematic atmospheric deflections of the laser beam, and systematic array survey errors.

The GLAS error budget for unmeasured high-frequency vibration in beam pointing is 0.45 arcsec (1σ), and is included in the 1.5 arcsec total pointing determination error budget (Bae and Schutz 1999). As the purpose of the calibration is to detect 1.5-arcsec-level or greater bias in the beam pointing, based on information of 1.5-arcsec or better accuracy, zero-mean random beam jitter of this level should have only a small effect on detecting this level of bias, given a sufficient number of calibration samples.

Simple computations were performed to assess the likely magnitude of impacts to the calibration due to atmospheric refraction of the GLAS laser beam (with a near-infrared wavelength of 1.064 μm, corresponding to the GLAS transmitter). This was done by applying Snell's Law to a column of air 100 km high, assuming an exponential density profile versus altitude, with standard temperature and pressure conditions at sea level. As expected from Snell's Law, off-nadir beam pointing was corrected towards nadir by the effect of refraction. The magnitude of the beam deflection from this "static-atmosphere" analysis was seen to be less than 0.01 arcsec (Lisano 1995).

Systematic array survey errors could have a potential impact on the accuracy of array-based calibration techniques. From trigonometry, each meter of bias in the array survey due to systematic errors results a calibration bias of 0.34 arcsec. According to Neumann et al. (1996), the use of precision GPS survey techniques should result in WGS-84 survey biases in the horizontal direction not worse than 10 cm, or 0.034 arcsec of pointing calibration bias.

9 Detector array size

Building and operating a detector array will include such activities as surveying the array site, maintaining the

array between calibration epochs, and possibly moving sections of the array, or the entire array, to increase the likelihood of an ICESat overflight. The total number of detectors in the array will impact on operational complexity, along with the overall hardware cost of the array. Determining the number of detectors required for the array depends on the following:

(1) cross-track array dimension, which depends primarily upon the uncertainty in the control of the altimeter beam pointing;
(2) along-track dimension, dependent upon the desired number of footprints to be detected;
(3) element spacing, which determines the desired level of accuracy with which the footprint centroid is to be geolocated.

The cross-track width is calculated to provide a 3-σ likelihood-of-detection criterion, accounting for ± 20 arcsec of pointing control accuracy. The resulting cross-track and along-track array dimensions are given in Table 6. Also given are three element spacings picked to minimize the number of elements required to use a particular method while also achieving 4.5-m centroid-determination accuracy 95% of the time. Based on the TMO/TMSD curve in Fig. 6, using Method 1 with an element spacing of 20 m will yield a footprint location accuracy of 2.43 $\pm$ 1.72 m (2σ). Similarly, based on the TMO/TMSD curve in Fig. 8, using Method 2 with an element spacing of 34 m will yield a footprint location accuracy of 0.5 $\pm$ 0.8 m (2σ). Also, based on the curve in Fig. 7, using Method 3 with an element spacing of 22 m will yield a footprint location accuracy of 0.25 $\pm$ 0.5 m (2σ).

Footprint centroid estimate accuracy of 4.5 m (1σ), required for 1.5-arcsec 1-σ calibration accuracy, is surpassed in each of the three methods which use data from photodetector arrays, even considering sizeable random errors in the intensity model and element survey in the intensity data case. Using the array dimensions and the element spacings given in Table 6, the estimated number of detectors required to detect one, two, and three footprints are computed, and are presented in Table 7.

The two-number sets in parentheses in Table 7 are the number of elements in the array in the cross-track and along-track directions, respectively. The third number is their product, i.e. the total number of elements in the array. These results can be used in designing the construction and maintenance of a calibration array. The results also demonstrate that measuring the intensity of the laser wavefront, versus collecting only on/off data, can considerably reduce the number of array elements, while improving calibration precision. Reducing the number of array elements in this way will in turn reduce the cost and complexity of building and operating an array.

Table 6. Array width, depth and spacing for array sizing

Cross-track array width for 3-σ likelihood of detection	
• For $\pm$60 m 1-σ cross-track off-nadir pointing accuracy	360 m
Along-track array depth for 100% likelihood of detection	
• For one 70-m-diameter footprint	240 m
• For two 70-m-diameter footprints	410 m
• For three 70-m-diameter footprints	580 m
Element spacings	
• On/off data only (4.15-m accuracy, 2σ = 1.4 arcsec)	20 m
• Intensity data, Method 2 (2.3-m accuracy, 2σ = 0.8 arcsec)	34 m
• Intensity data, Method 3 (0.75-m accuracy, 2σ = 0.25 arcsec)	22 m

Table 7. Number of array elements versus number of footprints detected and processing method, with expected 2-σ accuracy

Footprints detected	Method 1 (1.4-arcsec accuracy)	Method 2 (0.8-arcsec accuracy)	Method 3 (0.25-arcsec accuracy)
1	(18 × 12) 216	(11 × 8) 88	(17 × 11) 187
2	(18 × 21) 378	(11 × 13) 143	(17 × 19) 323
3	(18 × 29) 522	(11 × 18) 198	(17 × 27) 459

10 Conclusions

We assessed two approaches for calibrating satellite laser altimeter pointing with 1-arcsec-level or better precision. One approach, termed "topographic-inferred", generates estimates of the beam pointing angle by using altimeter height measurements, satellite position information, and a tract of surveyed terrain. The second approach, termed "direct detection", provides estimates of the beam pointing angle by sensing altimeter footprints on the ground. This approach is rendered accurate at the arcsecond level by use of a ground-based array of photodetectors, in a "ground-camera" approach. The centroids of the footprints are computed based on "on/off" or intensity measurements. These reference centroid estimates are used to calibrate the footprint centroid location computed using the vector sum of the satellite position and the altimeter measurement vector.

A Monte-Carlo evaluation of the topographic-inferred approach demonstrates that it can yield 1.5-arcsec calibration precision (1σ) for terrain sloped by 2° or more. In addition, the terrain slope must vary in direction with respect to the ICESat ground-track, to eliminate any ambiguity in the direction of the recovered pointing errors. The strength of the topographic technique is that, for a sufficiently large test area, it provides the opportunity to verify or validate the pointing angle for numerous pulses (5.88 pulses per kilometer of surveyed terrain along the ICESat ground-track).

The strength of the direct-detection approach, on the other hand, is that it potentially provides a more precise reference angle than the topographic approach. A parametric simulation study indicates that arcsecond-level calibration accuracy can be achieved by direct detection of footprints. However, direct detection also requires a substantial amount of hardware in order to detect and geolocate a few footprints.

Estimating the footprint centroid based on the locations of illuminated detectors (Method 1, using "on/off data") yields calibration potentially more accurate than the required level of 1.5 arcsec. Attaining this accuracy level using on/off data requires that the array elements be spaced no more than 20 m apart.

We also devised and demonstrated methods for improving the calibration precision to 0.5 arcsec or better, with a decreased number of detector array elements, based on measuring the footprint intensity at each reflector. Our studies indicate that intensity-based methods (Methods 2 and 3) are potentially several times more precise than Method 1, based on using data from fewer detectors than Method 1 requires. However, Methods 2 and 3 are presented here only as concept prototypes for intensity-based calibration, rather than the definitive plan for GLAS. This is because at the time the intensity methods were being assessed, the actual far-field intensity profile of the GLAS laser was not yet known. Other factors limiting the precision of the intensity-measurement calibration method are (1) unmodeled spatial variations in the wavefront intensity distribution, the largest of which will result from scintillation of the wavefront due to atmospheric turbulence, and (2) the level of background infrared noise at the altimeter beam wavelength.

A revised intensity-based method, using the actual GLAS intensity profile (which may be significantly non-Gaussian), could be assessed as a calibration approach, in view of the merits of the prototype intensity-based techniques described here. However, given the unpredictable degree of difficulty in adequately modeling the beam far-field intensity profile, the Method 1 technique using on-off data is clearly the more robust of the direct-detection calibration strategies for ICESat.

Both the Method 1 detector array approach and the topographic-inferred approaches theoretically enable detection of a 1.5-arcsec bias in the onboard beam pointing determination, based on as few as 10 footprint detection events. Using "Student-t" distributions for statistical tests of hypotheses with finite sample sets, we have determined 10 calibration data points to be a sufficient number of samples for detecting a 1.5-arcsec bias in the beam pointing determination, with 95% or better confidence of correct detection. In this assessment, we assumed the noise of the calibration data points (i.e. the difference between the onboard beam pointing determination estimate and the calibration pointing estimate) to have a standard deviation of $\sqrt{2} \times 1.5$ arcsec (the RSS of expected 1-σ beam pointing determination error and calibration error).

Even if a bias is detected between the calibration pointing estimate and the onboard beam pointing determination estimate, it is difficult to ascribe the bias to one estimate or the other, as both estimates have standard deviations of the same magnitude. Therefore, the best strategy for ICESat beam pointing calibration is to utilize two or more independent calibration approaches. In light of this, our recommendation is to use a combination of topographic and Method 1 array-based calibration.

Current plans for ICESat calibration are to experimentally implement both the direct-detection and topographic-inferred calibration approaches during the calibration period. Candidate sites for topographic-inferred calibration are being considered for their location along the 8-day ICESat calibration period repeat orbit, as well as undulating topography, to provide a range of terrain slope magnitudes and directions. A candidate site is the Mali sand dunes in Africa, centered approximately 17.5°N, 7.2°W (Schutz 1998b). Additionally, plans are being made for the use of ground detector arrays, and also direct aerial imaging of ICESat/GLAS footprints, over flat surfaces such as the Space Shuttle landing facility at White Sands, New Mexico (Schutz 1998a).

Acknowledgements. The research reported in this paper was performed under NASA Goddard Space Flight Center contract number NAG5-33021, with the University of Texas at Austin Center for Space Research.

References

Bae S, Schutz BE (1999) GLAS algorithm theoretical basis document version 2.0: precision attitude determination (PAD). University of Texas Center for Space Research, Austin, TX, pp 64–65

GLAS Science Team (1997) GLAS science requirements, version 2.1. Memorandum, NASA Goddard Space Flight Center, Greenbelt, MD

Lisano M (1995) Arcsecond-level calibration of satellite laser altimeter pointing with a ground-based electro-optical array and GPS. Dissertation, The University of Texas at Austin, Austin, TX

Neumann J, Manz A, Ford T, Mulyk O (1996) Test results from a new 2 cm real time kinematic GPS positioning system. Institute of Navigation, Sept. 1996, Proc ION GPS-96, Kansas City, KA pp. 873–882

Rim H, Davis G, Schutz B (1996) Dynamic orbit determination for the EOS laser altimeter satellite using GPS measurements. Journal of Astronantheal Sciences 44(3): 409–424

Schutz B (1998a) Spaceborne laser altimetry: 2001 and beyond. In: Plag HP (ed) Book of extended abstracts, WEGENER-98. Norwegian Mapping Authority, Honefoss, Norway

Schutz BE (1998b) GLAS validation plan version 0.1. University of Texas at Austin, Austin, TX

Schutz B, Lisano M, Davis G, Watkins M, Powell G (1994) Precision orbit determination for the EOS laser altimeter satellite (EOS-ALT/GLAS). AAS/AIAA Spaceflight Mechanics Meeting Paper 94-144, Cocoa Beach, FL Feb. 1994

Siegman A (1986) Lasers. University Science Books, Mill Valley, CA

Zwally H, Thomas R, Bindshadler R (1981) Ice-sheet dynamics by satellite laser altimetry. Institute of Electrical and Electronic Engineers 1981. Proc IGARSS '81, Washington DC, pp 1012–1022